

Quantifying the Impact of LSST *u*-band Survey Strategy on Photometric Redshift Estimation and the Detection of Lyman-break Galaxies

JOHN FRANKLIN CRENSHAW ^{1,2} BORIS LEISTEDT ³ MELISSA LYNN GRAHAM ² CONSTANTIN PAYERNE ⁴
ANDREW J. CONNOLLY ^{2,5} ERIC GAWISER ⁶ TANVEER KARIM ^{7,8} ALEX I. MALZ ⁹ JEFFREY A. NEWMAN ¹⁰
MARINA RICCI ¹¹ AND THE LSST DARK ENERGY SCIENCE COLLABORATION

¹*Department of Physics, University of Washington, Box 351560, Seattle, WA 98195*

²*DIRAC Institute, Department of Astronomy, University of Washington, Box 351580, Seattle, WA 98195*

³*Department of Physics, Imperial College London, Blackett Laboratory, Prince Consort Road, London SW7 2AZ, UK*

⁴*Université Paris-Saclay, CEA, IRFU, 91191, Gif-sur-Yvette, France*

⁵*eScience Institute, University of Washington, Box 351570, Seattle, WA 98195*

⁶*Department of Physics and Astronomy, Rutgers, the State University of New Jersey, Piscataway, NJ 08854, USA*

⁷*David A. Dunlap Department of Astronomy & Astrophysics, University of Toronto, 50 St George Street, Toronto, ON, M5S 3H4, Canada*

⁸*Dunlap Institute for Astronomy & Astrophysics, University of Toronto, 50 St George Street, Toronto, ON, M5S 3H4, Canada*

⁹*McWilliams Center for Cosmology and Astrophysics, Department of Physics, Carnegie Mellon University, Pittsburgh, PA, USA*

¹⁰*Department of Physics and Astronomy and PITT PACC, University of Pittsburgh, Pittsburgh, PA 15260, USA*

¹¹*Université Paris Cité, CNRS, AstroParticule et Cosmologie, F-75013 Paris, France*

ABSTRACT

The Vera C. Rubin Observatory will conduct the Legacy Survey of Space and Time (LSST), promising to discover billions of galaxies out to redshift 7, using six photometric bands (*ugrizy*) spanning the near-ultraviolet to the near-infrared. The exact number of and quality of information about these galaxies will depend on survey depth in these six bands, which in turn depends on the LSST survey strategy: i.e., how often and how long to expose in each band. *u*-band depth is especially important for photometric redshift (photo-*z*) estimation and for detection of high-redshift Lyman-break galaxies (LBGs). In this paper we use a simulated galaxy catalog and an analytic model for the LBG population to study how recent updates and proposed changes to Rubin’s *u*-band throughput and LSST survey strategy impact photo-*z* accuracy and LBG detection. We find that proposed variations in *u*-band strategy have a small impact on photo-*z* accuracy for $z < 1.5$ galaxies, but the outlier fraction, scatter, and bias for higher redshift galaxies varies by up to 50%, depending on the survey strategy considered. The number of *u*-band dropout LBGs at $z \sim 3$ is also highly sensitive to the *u*-band depth, varying by up to 500%, while the number of *griz*-band dropouts is only modestly affected. Under the new *u*-band strategy recommended by the Rubin Survey Cadence Optimization Committee, we predict *u*-band dropout number densities of 110 deg^{-2} (3200 deg^{-2}) in year 1 (10) of LSST. We discuss the implications of these results for LSST cosmology.

1. INTRODUCTION

The Vera C. Rubin Observatory’s Legacy Survey of Space and Time (LSST) will survey approximately $18,000 \text{ deg}^{-2}$ of the southern sky to unprecedented depth across such a wide area (Ivezić et al. 2019). This is made possible by an 8.4 m primary mirror and 3.2 Gigapixel camera, yielding an etendue significantly larger than any other existing telescope (LSST Science Collabora-

tion et al. 2009). Six photometric bands spanning the near-ultraviolet to near-infrared will provide information about the spectral energy distributions of objects detected by LSST, enabling, among other things, photometric redshift (photo-*z*) estimation for billions of galaxies. The quality of this information, however, depends on the depth in each of these bands, which in turn depends on the survey strategy. Of particular importance for static science is the number and length of visits to each field in the survey footprint.

Over many years, the Rubin Survey Cadence Optimization Committee (SCOC), in collaboration with the Rubin

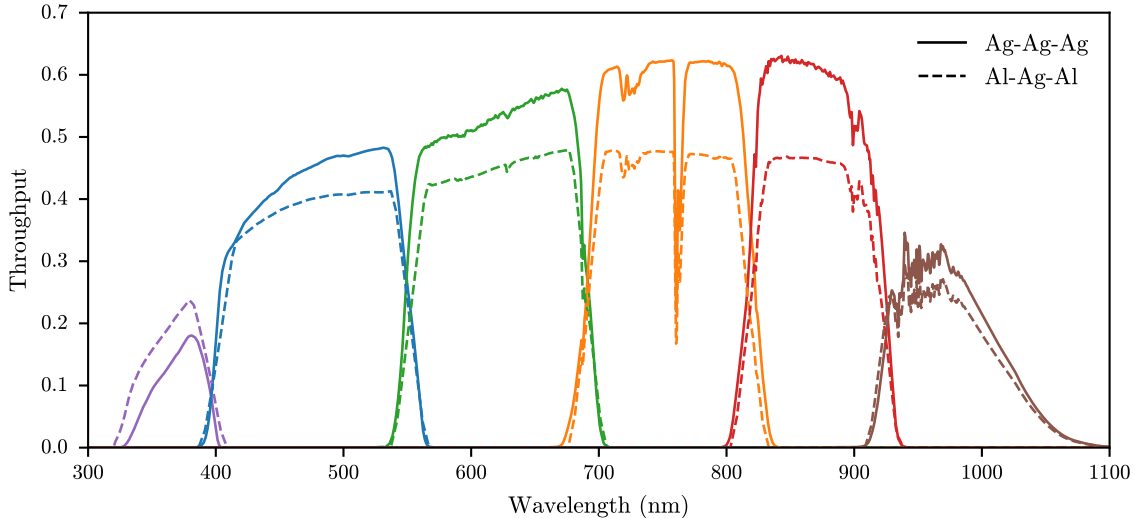


Figure 1. Comparison of Rubin Observatory *ugrizy* throughput curves, assuming original Al-Ag-Al and new Ag-Ag-Ag mirror coatings. The transition to all-silver coatings decreased throughput in the *u* band, but increased throughput in all of the *grizy* bands. These curves include contributions from the atmosphere (assuming airmass 1.2), mirror reflectivities, lens and filter throughputs, and detector sensitivity.

science community, has refined LSST survey strategy to maximize Rubin’s science potential, while balancing the needs of a diverse set of science cases (e.g., [LSST Science Collaboration et al. 2017](#); [Jones et al. 2021](#); [Rubin Observatory Survey Cadence Optimization Committee 2022, 2023, 2024](#); [Bianco et al. 2022](#); [Lochner et al. 2022](#)). This is an ongoing process that will continue throughout the 10 year duration of LSST. Recently, the decision was made to change the coating of Rubin’s primary (M1), secondary (M2), and tertiary mirrors (M3)¹ from aluminum-silver-aluminum (Al-Ag-Al) to silver-silver-silver (Ag-Ag-Ag)². This change reduces the throughput in the ultraviolet (i.e., in Rubin’s *u* band), while increasing throughput at longer wavelengths (Rubin’s *grizy* bands; see Fig. 1). Because substantially more survey time is spent observing in *grizy* bands than in the *u* band alone, this results in greater survey efficiency, enabling deeper imaging by the end of LSST. Under the nominal survey strategy at the time of this change, however, the change in mirror coating reduced the 10-year *u*-band depth by 0.21 magnitudes.

The *u* band, spanning approximately 3300 - 4000 Å, is important for a variety of science cases. At low redshifts, the redshifting of the ~ 4000 Å Balmer break through the *u* band enables accurate photo-*z* estimation for galaxies at redshifts $z < 0.5$ ([Kalmbach et al. 2020](#)).

¹ Rubin’s primary and tertiary mirrors are a singular structure, usually referred to as the M1M3.

² Note this decision was made before the mirrors were ever coated, so the M1M3 mirror was never actually coated with aluminum.

Without the *u* band, photo-*z*’s for these galaxies are highly uncertain, resulting in catastrophic outliers that significantly degrades photo-*z* estimation up to redshifts $z < 0.6$ ([LSST Science Collaboration et al. 2009](#)). This has implications for nearly every area of LSST cosmology, including lens and source selection for galaxy clustering and lensing analyses ([Schmidt et al. 2020](#); [Zuntz et al. 2021](#); [Zhang et al. 2023](#); [Leonard et al. 2024](#)), galaxy cluster detection ([Euclid Collaboration et al. 2019](#)), supernova cosmology ([Chen et al. 2022, 2024](#); [Mitra et al. 2023](#)). Achieving precision cosmology therefore places stringent constraints on photo-*z* performance ([The LSST Dark Energy Science Collaboration et al. 2018](#); [Newman et al. 2015](#); [Newman & Gruen 2022](#)).

At higher redshifts, Lyman-series absorption lines shift into the *u* band, beginning with the Lyman-alpha transition at rest-frame 1216 Å, which redshifts into the *u* band at $z \sim 1.7$, and culminating with the Lyman-limit at rest-frame 912 Å, which redshifts into the *u* band at $z \sim 2.6$. These features, caused by absorption from neutral hydrogen in the intergalactic medium (IGM) and within the galaxies themselves, enable identification and photo-*z* estimation for high-redshift star-forming galaxies known as Lyman-break galaxies (LBGs; [Steidel et al. 1996](#)).

For thirty years, LBGs have been important for studies of galaxy formation and evolution ([Giavalisco 2002](#); [Dunlop 2013](#)), including the ultra-high-redshift LBGs discovered in recent years by JWST, illuminating galaxy formation at cosmic dawn (e.g., [Finkelstein et al. 2022](#); [Mason et al. 2022](#); [Harikane et al. 2023](#)). LBGs, however,

are also increasingly being recognized as cosmologically important tracers of the matter density field at high redshifts. With the width and depth of LSST, using LBGs as cosmological tracers has the potential to provide unprecedented constraints on the growth of structure and evolution of dark energy at redshifts $2 < z < 6$ (Wilson & White 2019; Miyatake et al. 2022); competitive constraints on the amplitude of local-type primordial non-Gaussianity (Schmittfull & Seljak 2018; Chaussidon et al. 2024); constraints on the sum of neutrino masses, independent of the optical depth of reionization (Yu et al. 2018); constraints on the masses of $z > 1$ clusters (Tudorica et al. 2017); and constraints on the low-redshift matter density field via inverse galaxy-galaxy lensing (IGGL; Cross & Sánchez 2024).

The u -band dropout technique, which selects galaxies with a strong u -band flux deficit compared to the g or r band flux, is especially effective at selecting LBGs at redshifts $2 < z < 4$. The success of this technique is strongly dependent on u -band depth. By selecting u -band dropouts in images from the CFHT Large Area u -band Survey (CLAUDS; Sawicki et al. 2019) and deep grz imaging from Hyper Suprime Cam Subaru Strategic Program (HSC SSP; Aihara et al. 2019), Ruhlmann-Kleider et al. (2024) demonstrated it is possible to achieve a spectroscopically-confirmed $2.3 < z < 3.5$ LBG number density of 620 deg^{-2} , from an initial photometric sample of $1,100 \text{ deg}^{-2}$ with $r < 24.2$. The 10-year LSST Wide Fast Deep (WFD) survey, however, will be shallower than the CLAUDS and HSC SSP deep fields. More recently, Payerne et al. (2024) employed a refined LBG selection method on shallower imaging, simulating the ongoing Ultraviolet Near Infrared Optical Northern Survey (UNIONS, Gwyn et al., in prep.) which will have a depth similar to LSST year 2. This work achieved a confirmed LBG number density of 493 deg^{-2} within $2 < z < 3.5$ from a photometrically-selected sample of $1,100 \text{ deg}^{-2}$ with $r < 24.3$, providing valuable insights into LSST’s near-future potential for probing dark energy, growth of structure, and primordial non-Gaussianity.

It is therefore essential to understand how LSST survey strategy impacts u -band depth and the corresponding implications for photo- z estimation and high-redshift cosmology. Due to the increased survey efficiency provided by the Ag-Ag-Ag mirror coatings, it is possible to allocate observing time in each band such that the coadded depths in all bands are deeper than the nominal depths assuming the original Al-Ag-Al mirror coatings. The question, therefore, is how to best balance the depths in each of the six bands to optimize photo- z estimation and LBG detection. In this paper, we use simulations and simple analytic models to address these questions.

Table 1. Summary of notation used in paper

Notation	Description
u, g, r, i, z, y	Apparent magnitudes in LSST bandpasses
u_N, g_N, \dots	$N\sigma$ limit in LSST bandpasses
$u_{\text{cut}}, g_{\text{cut}}, \dots$	Cuts applied to LSST bandpasses
m	Apparent magnitude in an arbitrary band
m_N	$N\sigma$ limit in an arbitrary band
m_{cut}	Cut applied to an arbitrary band
M	Absolute magnitude at rest-frame 1500 \AA
“Dropout band”	Bandpass in which the Lyman-break falls (i.e., containing $(1+z)912 \text{ \AA}$)
“Detection band”	Bandpass closest to rest-frame 1500 \AA (i.e., closest to $(1+z)1500 \text{ \AA}$)

NOTE— All magnitudes are in the AB system; for $ugriz$ -dropouts, the detection bands are *rizzly*, respectively.

Section 2 details the simulations and models used in this paper. In Section 3 we describe the metrics used to quantify photo- z performance and LBG detection for different observing strategies, the results of which are presented in Section 4. We discuss the implications of our results for LSST cosmology and conclude in Section 5.

We assume Planck Collaboration et al. (2020) cosmology throughout. We use AB magnitudes, and refer to apparent magnitudes, N -sigma depths, and cuts in LSST bands as u, u_N, u_{cut} , etc. We use lowercase m to refer to apparent magnitudes in arbitrary bands (i.e. any of *ugrizy*), and uppercase M to refer to absolute magnitudes at rest-frame 1500 \AA . For each LBG dropout sample, we use “dropout band” to refer to the Rubin band in which the redshifted Lyman-break falls, and “detection band” to refer to the band closest to rest-frame 1500 \AA . Specifically, for *ugriz* dropout samples, the dropout bands are *ugriz* and the detection bands are *rizzly*. This notation is summarized in Table 1.

Finally, we note this paper contributes to an ongoing literature studying how survey strategy impacts photo- z estimation, including Graham et al. (2018); Lochner et al. (2018); Graham et al. (2020); Malz et al. (2021); Lochner et al. (2022); Scott et al. (2024); Hang et al. (2024).

2. SIMULATIONS AND IGM + LBG MODELS

Different survey strategies are simulated using the Rubin Observatory Operations Simulator, described in Section 2.1. The impact on photo- z estimation is studied using a simulated galaxy catalog, which is described in Section 2.2, including modeling the effects of IGM extinction in the u and g bands. High-redshift LBGs are

Table 2. *u*-band strategy variations to baseline v3.4

Strategy	Relative <i>u</i> time	Δu	Δg	Δr	Δi	Δz	Δy
1.0x, 30s <i>u</i>	1.00	0.00 (0.00)	0.00 (0.00)	0.00 (0.00)	0.00 (0.00)	0.00 (0.00)	0.00 (0.00)
1.0x, 38s <i>u</i>	1.27	0.20 (0.18)	0.00 (-0.01)	-0.04 (-0.01)	-0.02 (-0.01)	0.02 (-0.01)	-0.01 (-0.00)
1.0x, 45s <i>u</i>	1.50	0.32 (0.31)	-0.03 (-0.01)	-0.05 (-0.02)	-0.03 (-0.02)	0.00 (-0.02)	-0.02 (-0.01)
1.0x, 60s <i>u</i>	2.00	0.56 (0.52)	-0.08 (-0.04)	-0.07 (-0.04)	-0.05 (-0.03)	-0.02 (-0.04)	-0.04 (-0.02)
1.1x, 30s <i>u</i>	1.10	0.02 (0.04)	-0.01 (-0.01)	-0.02 (-0.00)	-0.01 (-0.01)	0.02 (0.00)	-0.00 (-0.00)
1.1x, 38s <i>u</i>	1.39	0.20 (0.24)	-0.01 (-0.02)	-0.03 (-0.01)	-0.02 (-0.01)	0.01 (-0.01)	-0.01 (-0.00)
1.1x, 45s <i>u</i>	1.65	0.31 (0.36)	-0.04 (-0.02)	-0.04 (-0.02)	-0.02 (-0.02)	-0.00 (-0.02)	-0.01 (-0.01)
1.1x, 60s <i>u</i>	2.20	0.56 (0.55)	-0.07 (-0.04)	-0.09 (-0.04)	-0.05 (-0.04)	-0.02 (-0.04)	-0.04 (-0.02)
1.2x, 30s <i>u</i>	1.20	0.04 (0.09)	-0.01 (-0.01)	-0.02 (-0.01)	-0.01 (-0.01)	0.03 (-0.01)	-0.01 (-0.01)
1.2x, 38s <i>u</i>	1.52	0.25 (0.29)	0.00 (-0.03)	-0.03 (-0.02)	-0.03 (-0.02)	-0.01 (-0.02)	-0.01 (-0.01)
1.2x, 45s <i>u</i>	1.80	0.37 (0.41)	-0.03 (-0.03)	-0.06 (-0.02)	-0.04 (-0.03)	0.02 (-0.03)	-0.03 (-0.02)
1.2x, 60s <i>u</i>	2.40	0.56 (0.61)	-0.09 (-0.05)	-0.07 (-0.04)	-0.06 (-0.05)	-0.03 (-0.05)	-0.05 (-0.04)
1.5x, 30s <i>u</i>	1.50	0.10 (0.22)	-0.00 (-0.01)	-0.03 (-0.02)	-0.03 (-0.04)	0.01 (-0.01)	-0.00 (-0.01)
1.5x, 38s <i>u</i>	1.90	0.28 (0.40)	-0.02 (-0.04)	-0.04 (-0.04)	-0.02 (-0.04)	0.00 (-0.03)	-0.01 (-0.02)
1.5x, 45s <i>u</i>	2.25	0.41 (0.53)	-0.06 (-0.05)	-0.07 (-0.04)	-0.05 (-0.05)	-0.02 (-0.04)	-0.03 (-0.03)

NOTE— The second column quantifies the time spent observing in the *u* band, relative to the baseline v3.4 observing strategy. The right six columns display changes in year 1 (10) *ugrizy* median 5σ depths for the WFD survey. For comparison, the median 5σ depths for the [1.0x, 30s *u*] strategy are 24.04 (25.15), 25.48 (26.65), 25.69 (26.84), 25.29 (26.40), 24.53 (25.73), 23.68 (24.78) for *ugrizy* in year 1 (10), respectively. Note that the [1.0x, 30s *u*] strategy is the same as baseline v3.4.

studied using an analytic model, described in Section 2.3, which enables consistent comparison between observing strategies and obviates the need for a simulated high-redshift catalog.

2.1. Rubin Operations Simulator

The Rubin Observatory Operations Simulator³ (OpSim) generates mock observations over the 10-year duration of LSST. These simulations include telescope movement, dithering, variable weather and seeing conditions drawn from a Cerro-Tololo Inter-American Observatory (CTIO) historical log, and simulated downtime due to weather and maintenance. OpSim outputs are processed by the Metrics Analysis Framework (MAF; Jones et al. 2014) which computes spatially-varying summary statistics (e.g. median seeing) and derived metrics (e.g. coadded 5σ depths) that are used to assess survey strategy with regards to survey efficiency and various science drivers.

We primarily focus on the LSST Wide Fast Deep (WFD) survey, which excludes areas with high galactic extinction ($E(B-V) > 0.2$). We use maps of extragalactic extinction-corrected coadded 5σ point source depths: $\{u_5, g_5, r_5, i_5, z_5, y_5\}$. These maps are in HEALPix

(Górski et al. 2005) format with $N_{\text{side}} = 128$, corresponding to a pixel size of 755 arcmin².

To quantify the impact of *u*-band strategy, we compare a series of recent “baseline” simulations,

- baseline v3.4: fiducial simulation of LSST including throughputs for the Ag-Ag-Ag mirror coatings, using band allocations identical to the most recent Al-Ag-Al fiducial simulation.
- baseline v3.5: an update to baseline v3.4 that includes 10% more visits with 38 second exposures in the *u* band (compared to previous 30 second exposures), as well as the uniform rolling strategy (see Rubin Observatory Survey Cadence Optimization Committee (2024)).
- baseline v3.6: an update to baseline v3.5 that includes a more realistic estimate of observatory downtime in year 1 (8 weeks), reducing the number of visits by $\sim 5\%$, as well as an improved model of mechanical inefficiencies in telescope slewing.
- baseline v4.0: an update to baseline v3.6 that includes minor bugfixes to the year 1 downtime that result in slightly more observation time in year 1.

In addition to these baseline strategies, we analyze a suite of variations to baseline v3.4 that vary only the

³ <https://rubin-sim.lsst.io/>

u -band observing allocation, while simultaneously adjusting the $grizy$ allocations to maintain the 10-year duration of LSST (i.e. increasing u -band observing time necessitates decreasing $grizy$ observing time, which are each decreased by the same proportion). These strategies include increasing the number of u -band visits by 10%, 20%, and 50%, while setting the per-visit exposure time to 30, 38, 45, and 60 seconds. Throughout, we refer to these strategies with names such as [1.1x, 38s u], which refers to the strategy that increases u -band visits by 10% and the per-visit exposure time to 38 seconds. Table 2 lists each of these simulated variations, their relative change in overall u -band exposure time, and their impact on median depth in each band. Note that for the same amount of u -band observing time, strategies with longer per-visit exposures yield greater depth in the u band compared to more visits with shorter exposures. This is because noise in the u band is dominated by read noise and not sky background due to the fainter sky background in the ultraviolet. Also note that the [1.0x, 30s u] strategy is the same as baseline v3.4. Baselines v3.5 onward have adopted the [1.1x, 38s u] strategy, partially as a result of the findings presented here, but these simulations are not identical to the baseline v3.4 [1.1x, 38s u] simulation due to the other changes described above.

Finally, in addition to the WFD forecasts we make for every survey strategy, for the baseline v4.0 simulation we also estimate LBG number densities in the LSST Deep Drilling Fields (DDFs): COSMOS, the Extended Chandra Deep Field South (ECDFS), ELAIS S1, XMM-LSS, and the Euclid Deep Field South (EDFS). The DDFs are typically 1.3 magnitudes deeper in each band than the WFD survey, however EDFS is shallower than the others as it receives approximately the same number of visits spread over roughly twice the area. COSMOS, furthermore, has an accelerated schedule to build significant depth within the first 3 years to aid cosmology systematics calibration and low-surface-brightness science.

2.2. Simulating IGM extinction for $z \leq 3.5$ Galaxies

For our studies of photo- z accuracy we use a simulated catalog based on the Millennium simulation (Springel et al. 2005), using the GALFORM semi-analytic galaxy formation model (Gonzalez-Perez et al. 2014) and the lightcone construction techniques described by Merson et al. (2013). This catalog was designed to model the optical and near-infrared properties, including emission lines, of $z \leq 3.5$ galaxies detected by LSST. We apply a magnitude cut of $m_i < 25.5$, which is slightly deeper than the DESC gold sample (The LSST Dark Energy

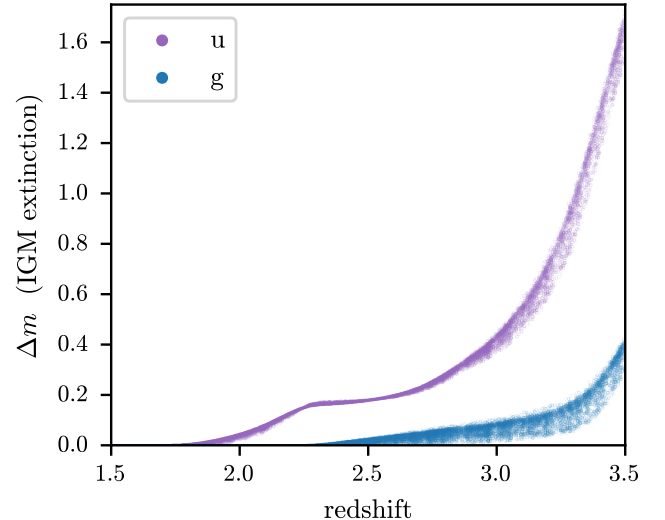


Figure 2. IGM magnitude increments in the Rubin u and g bands for $z > 1.5$ galaxies in the simulated catalog. The scatter is due to scatter in UV slope, β_{UV} .

Science Collaboration et al. 2018) to avoid edge effects in our analysis.

This catalog contains true redshifts and $ugrizy$ magnitudes for 240,000 galaxies⁴. The model that generated these true magnitudes includes Lyman-series absorption in the atmospheres of these galaxies, but does not include the effects of extinction in the intergalactic medium (IGM), which also absorbs rest-frame UV flux from these galaxies as photons travel through neutral hydrogen clouds along the line-of-sight. This effect, commonly named the Lyman-alpha forest, is redshift and wavelength dependent, and therefore provides valuable information for photo- z estimation in addition to the information provided by Lyman-series absorption intrinsic to galactic atmospheres. As this information redshifts into the Rubin u band at $z > 1.6$ (and the g band at $z > 2.2$), we wish to model this missing IGM absorption to maximize the utility of the u band for photo- z estimation in our simulations.

We use the following model to add IGM extinction at the catalog level. Consider a galaxy with observed-frame SED $f_\lambda(\lambda) \equiv f_\lambda(\lambda, z) \propto f_\lambda(\lambda/(1+z), z=0)$, observed in a bandpass with transmission⁵ $R_m(\lambda)$. In the absence of IGM extinction (e.g., in our simulated catalog), we

⁴ These true magnitudes were computed for the original A1-Ag-A1 throughputs. The new throughputs have nearly identical shapes, however, with only the normalization being substantially different. These true magnitudes are, therefore, still valid for the new throughputs.

⁵ This is the dimensionless throughput, giving the probability that a photon with wavelength λ will be detected.

observe the magnitude

$$m = -2.5 \log_{10} f + c_m$$

where $f = \int f_\lambda(\lambda) R_m(\lambda) \lambda d\lambda$, (1)

and c_m is a band-dependent constant. However, if we include the observed-frame IGM transmission $T(\lambda)$, we observe the magnitude

$$m_{\text{wIGM}} = -2.5 \log_{10} f_{\text{wIGM}} + c_m$$

where $f_{\text{wIGM}} = \int T(\lambda) f_\lambda(\lambda) R_m(\lambda) \lambda d\lambda$. (2)

Absorption in the IGM, therefore, effectively increments observed magnitudes by the amount

$$\Delta m_{\text{wIGM}} = m_{\text{wIGM}} - m = -2.5 \log_{10} \frac{f_{\text{wIGM}}}{f}. \quad (3)$$

We wish to compute these IGM corrections for the galaxies in our catalog.

If we assume the UV SED for each galaxy can be approximated by a power law, $f_\lambda(\lambda) \propto \lambda^{\beta_{\text{UV}}}$ where β_{UV} is the ‘‘UV slope’’, the flux ratio is then

$$\frac{f_{\text{wIGM}}}{f} = \int T(\lambda) \tilde{R}_m(\lambda) d\lambda \quad (4)$$

where

$$\tilde{R}_m(\lambda) = \frac{\lambda^{\beta_{\text{UV}}+1} R_m(\lambda)}{\int \lambda^{\beta_{\text{UV}}+1} R_m(\lambda) d\lambda}. \quad (5)$$

The IGM correction Δm_{wIGM} , then, depends only on the UV slope β_{UV} .

For this simple model, we fit β_{UV} from the $u - g$ color of the galaxies. Assuming the u -band flux is the flux of the galaxy at the effective wavelength of the u band,

$$\lambda_u = \frac{\int \lambda f_\lambda(\lambda) R_u(\lambda) \lambda d\lambda}{\int f_\lambda(\lambda) R_u(\lambda) \lambda d\lambda} \quad (6)$$

we have

$$u \sim -2.5 \log_{10} \lambda_u^{\beta_{\text{UV}}+2} + c_u + c, \quad (7)$$

where c is a band-independent constant. Similar equations holds for the g band. We then estimate the UV slope from the $u - g$ color:

$$\beta_{\text{UV}} = (u - g) \left(-2.5 \log_{10} \frac{\lambda_u}{\lambda_g} \right)^{-1} - 2. \quad (8)$$

Note however, that this definition is circular, as the effective wavelength depends on the UV slope. We, therefore, estimate initial effective wavelengths assuming

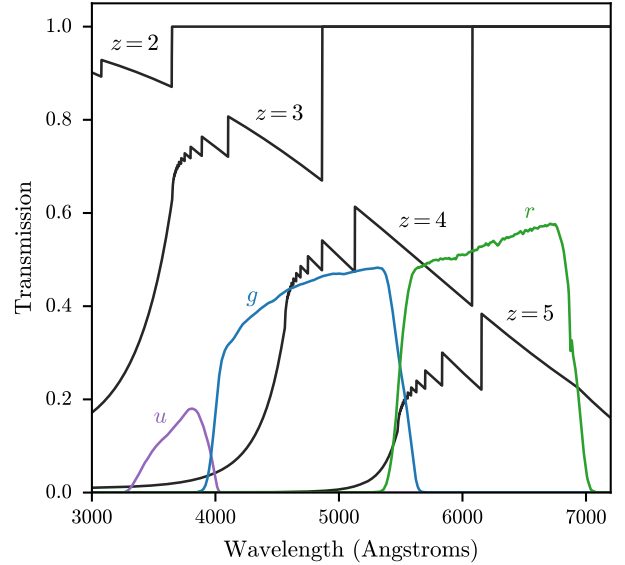


Figure 3. Transmission of the IGM in black, plotted for several different source redshifts. The transmission of the LSST photometric bandpasses (with Ag-Ag-Ag coating) are plotted in color to help visualize how much IGM extinction impacts each band at different redshifts.

$\beta_{\text{UV}} = -2$, estimate new values for β_{UV} , and iterate until convergence. For our simulated catalog, final estimates of β_{UV} range from -4 for extreme star formers, to 8 for very red galaxies. The bottom of this range matches expectations for extreme star-forming galaxies [Bouwens et al. \(2014\)](#); [Izotov et al. \(2021\)](#). We have not found published estimates of UV slopes for red galaxies, as this is a technique typically used for studying star formation. We note, however, that the UV slope provides only a modest modulation to the mean IGM extinction, as seen in Fig. 2, so we do not expect this simple model to endanger any conclusions of this paper.

We use the [Inoue et al. \(2014\)](#) analytic $\tau(\lambda, z)$ model of IGM optical depth to model IGM transmission $T(\lambda, z) = e^{-\tau(\lambda, z)}$. Figure 3 plots the three bluest Rubin bandpasses together with the IGM transmission for a few different source redshifts. The galaxies in our simulated catalog are all at $z \leq 3.5$, for which only the u and g band see any significant IGM extinction.

Finally, Δm_{wIGM} for galaxies in the simulated catalog are plotted in Figure 2. The dispersion in Δm_{wIGM} is due to the UV slopes of the galaxies. Whether points above (below) the mean are bluer (redder) than average depends on the source redshift. See Appendix A for more details.

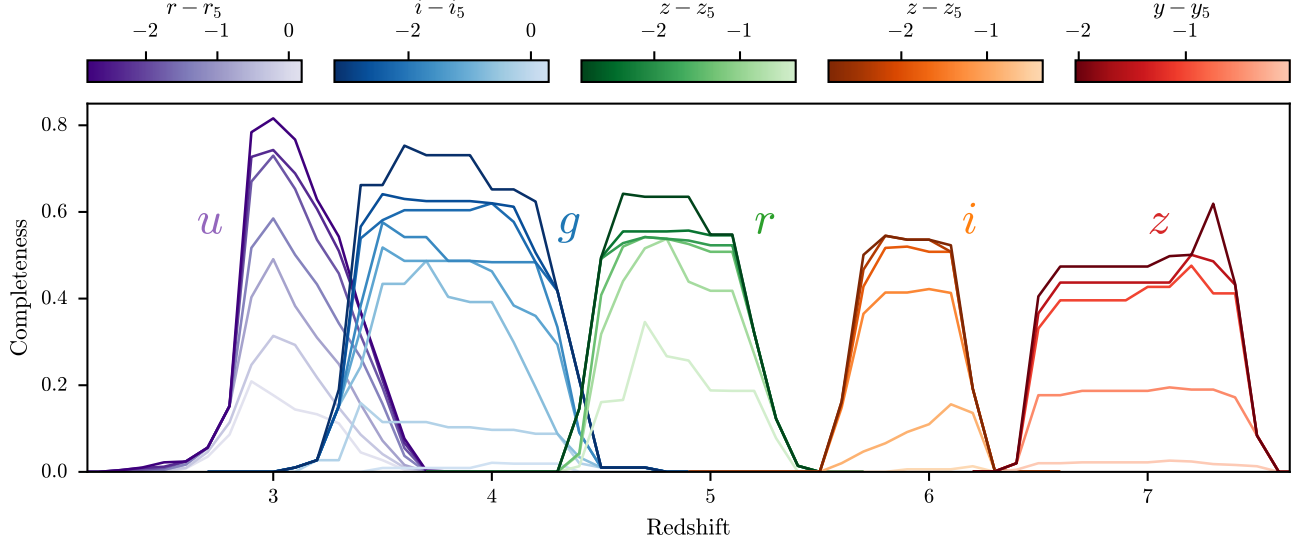


Figure 4. LBG completeness curves for *ugriz* dropouts (labeled in the main panel) as a function of redshift, in bins of LBG magnitude relative to the 5σ depth in the detection band (color coded according to the bars above the main panel). *u*-dropout completeness comes from Malkan et al. (2017); *griz* completeness comes from Ono et al. (2018); Harikane et al. (2022).

2.3. LBG Flux and Population Model

We model the intrinsic rest-frame spectra of LBGs in absolute magnitudes using a power law,

$$f_{\lambda}^{\text{intr}}(\lambda, M, z) = A \cdot 10^{-0.4M} \left(\frac{\lambda}{1500 \text{ \AA}} \right)^{\beta_{\text{UV}}(M, z)}, \quad (9)$$

where M is the absolute magnitude at 1500 \AA ⁶, and the normalization $A = 4.83 \times 10^{-8} \text{ erg s}^{-1} \text{ cm}^{-2} \text{ \AA}^{-1}$. The UV slope is calculated using the bilinear model

$$\beta_{\text{UV}}(M, z) = -0.167(M + 19.5) - 0.063z - 1.61, \quad (10)$$

which is fit to high-redshift Hubble data from Bouwens et al. (2014) (see Appendix B). The observed spectrum in apparent magnitudes, accounting for redshift and IGM extinction, is then

$$f_{\lambda}^{\text{obs}}(\lambda, M, z) = \frac{1}{1+z} \left(\frac{10 \text{ pc}}{D_L(z)} \right)^2 f_{\lambda}^{\text{intr}}(\lambda_e, M, z) T(\lambda, z) \quad (11)$$

where $D_L(z)$ is the luminosity distance to redshift z , and $\lambda_e = \lambda/(1+z)$ is the emitted wavelength. Finally, the observed bandpass magnitude is

$$m(M, z) = -2.5 \log_{10} \left(\frac{\int f_{\lambda}^{\text{obs}}(\lambda, M, z) R_m(\lambda) \lambda d\lambda}{\int f_{\lambda}^{\text{AB}}(\lambda) R_m(\lambda) \lambda d\lambda} \right), \quad (12)$$

⁶ I.e., M is the AB magnitude as calculated with the bandpass $R(\lambda) = \delta(\lambda - 1500 \text{ \AA})$, where δ is the Dirac delta function, assuming the galaxy is at 10 pc (for which redshift $z \sim 0$).

where $f_{\lambda}^{\text{AB}}(\lambda) = 0.109 (\lambda/\text{\AA})^{-2} \text{ erg s}^{-1} \text{ cm}^{-2} \text{ \AA}^{-1}$ is the AB reference spectrum (i.e. $f_{\nu} = 3631 \text{ Jy}$). Note that Equations 9-12 provide a fully-determined analytic model for m , the apparent magnitude in bandpass R_m , as a function of redshift, z , and the absolute magnitude at rest-frame 1500 \AA , M . Alternatively, by numerically inverting these equations, we have a fully-determined model for M as a function of z and m .

True LBG number density as a function of redshift and absolute magnitude at 1500 \AA (i.e., the luminosity function) is modeled using a double power law:

$$\phi(M, z) = \phi^* \left[10^{0.4(\alpha+1)(M-M^*)} + 10^{0.4(\beta+1)(M-M^*)} \right]^{-1}, \quad (13)$$

where ϕ^* is the characteristic number density, M^* is the characteristic magnitude, β is the bright-end slope, and α is the faint-end slope. For the redshift evolution of each parameter we use the following model:

$$\begin{aligned} \log \phi^*(z) &= -1.45 - 0.31(1+z) \\ M^*(z) &= -21.18 + 0.02(1+z) \\ \alpha(z) &= -1.27 - 0.11(1+z) \\ \beta(z) &= -4.79 + 0.05(1+z). \end{aligned} \quad (14)$$

These coefficients, from Table 2 of Finkelstein & Bagley (2022), are fit to a collection of data from CANDELS (Finkelstein et al. 2015; Parsa et al. 2016; Bouwens et al. 2021), the Hubble Frontier Fields (Bouwens et al. 2022), HSC SSP (Harikane et al. 2022), CLAUDS (Moutard et al. 2020), SHELA (Stevans et al. 2018), and UltraVISTA/VIDEO (Adams et al. 2020).

The fraction of true LBGs detected and classified as such by Rubin, as a function of redshift, observed magnitude in the detection band, and 5σ limiting depth in the detection band, is estimated using the LBG completeness models of Malkan et al. (2017); Ono et al. (2018); Harikane et al. (2022). In particular, the completeness is quantified in terms of $m - m_5$, the magnitude in the detection band, relative to the 5σ depth in the same band. For *ugriz*-dropout samples, we define the detection band as the Rubin bandpass closest to the redshifted $(1+z)1500 \text{ \AA}$: *rizzly*, respectively. Completeness models, for a discrete set of $m - m_5$ values in the detection band, are shown in Figure 4, from which it is clear that the dropout samples are less complete for galaxies with detection band magnitudes closer to the 5σ limit. For more details, see Appendix C.

Finally, we estimate detected LBG number densities by integrating the luminosity function and completeness model:

$$n = \int_0^\infty dz \frac{dV}{dz} \int_{-\infty}^{M_{\text{cut}}} dM \phi(M, z) C(M, z; M_5). \quad (15)$$

The absolute-magnitude cut, $M_{\text{cut}} = M_{\text{cut}}(m_{\text{cut}}, z)$, and the absolute-magnitude 5σ depth, $M_5 = M_5(m_5, z)$, are calculated from the detection-band apparent magnitude equivalents, m_{cut} and m_5 , by inverting Equation 12. Note that m_5 is the apparent magnitude corresponding to a flux with signal-to-noise ratio (SNR) of 5 in the detection band, which is provided by OpSim (see Section 2.1), while m_{cut} is the cut on apparent magnitude for LBGs selected for cosmology (see Section 3.2). Number densities as a function of detection-band m_5 (where we have set $m_{\text{cut}} = m_5$) are shown in Figure 5. Median depths for the baseline v4.0 survey strategy are marked, using bars, dots, and stars for WFD years 1 and 10, and COSMOS year 10, respectively.

We do not model contamination from low-redshift interlopers for the metrics presented in this work. Low-redshift interlopers, however, are very important for cosmology and astrophysics applications, and are discussed in Section 5.

3. METHODS

In this section we describe how we use the OpSim simulations of the LSST survey strategy to estimate photo- z 's for the simulated Millenium/GALFORM $z \leq 3.5$ catalog, and high-redshift LBG number densities using the analytic population and flux model.

3.1. Photo- z Estimation

To estimate photo- z 's for the $z \leq 3.5$ simulated catalog we use the Color-Matched Nearest-Neighbors (CMNN)

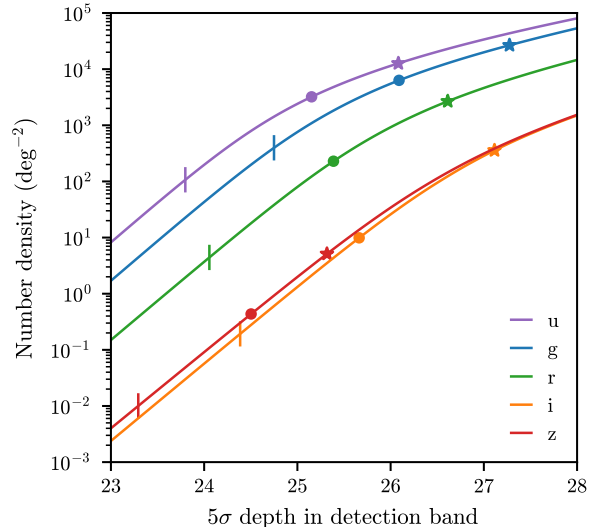


Figure 5. Projected number densities for *ugriz* dropouts as a function of magnitude cut in the detection band, assuming $m_{\text{cut}} = m_5$. Expected depths and number densities for the baseline v4.0 survey strategy are indicated by bars, dots, and stars for LSST WFD years 1 and 10, and COSMOS year 10, respectively.

algorithm (Graham et al. 2018, 2020). CMNN is not chosen because it is the best photo- z estimator, but rather because the accuracy and precision of CMNN estimates are straightforwardly related to the precision of the input photometry. This attribute makes the CMNN photo- z estimator useful for evaluating the relative change in photo- z performance due to varying photometric quality in different survey strategy simulations.

The CMNN estimator is described fully in Graham et al. (2018, 2020). To briefly summarize, it takes as input only two things: the median 5σ depths in each of the *ugrizy* bands for a given survey simulation, and the simulated galaxy catalog of true apparent magnitudes. Given the depths, it calculates observational magnitude uncertainties for every galaxy (using the error model described in Ivezić et al. 2019; Crenshaw et al. 2024), and then uses the errors to simulate observed apparent magnitudes (i.e., adds randomly generated noise to the true flux). The catalog is then split into a training set of 200,000 galaxies and a test set of 40,000 galaxies, and the training set is used to estimate a photo- z point estimate for each galaxy in the test set.

3.2. Forecasting Dropout Number Densities

Constraining large-scale structure with LBGs requires assembling a relatively uniform, high-number density sample across the largest possible area of the sky. These criteria are in tension, as uniformity and number density encourage selection of the deepest areas of the survey,

while sky area encourages selecting the widest possible area of the survey (cf. the trade-offs in [Ruhmann-Kleider et al. 2024](#) and [Payerne et al. 2024](#)). This trade-off between width and depth will need to be optimized for real analyses that seek to maximize cosmological constraining power. Furthermore, LBG selection criteria, which rely on colors that straddle the observed-frame Lyman-break at $\lambda_{\text{obs}} \sim 912 \text{ \AA} (1+z)$, will need to be optimized to balance sample size, completeness, and purity according to the needs of cosmology analyses ([Wilson & White 2019](#)). Here, we make a simple set of choices that enables consistent comparison between different observing strategies:

- we use the deepest 75% of the WFD footprint (corresponding to a sky fraction $f_{\text{sky}} = 0.32$);
- in the dropout band, magnitudes below the 3σ limit are replaced by 3σ lower bounds (i.e., magnitudes $m > m_3$ are replaced with m_3 , which is understood as a lower bound on the magnitude);
- we require that every LBG used for cosmology have $\text{SNR} > 5$ in the detection band;
- we set the dropout threshold to 1 magnitude; i.e. $m_{\text{dropout}} - m_{\text{detection}} \geq 1$.

These requirements are used to determine m_{cut} (defined in Section 2.3) as a function of the OpSim map for each survey strategy.

For u - and g -dropouts, the dropout band is not sufficiently deep⁷ with respect to the detection band (r and i , respectively), so that the dropout band is the limiting factor when determining magnitude cuts. For these samples, therefore, we select the deepest 75% of pixels in the *dropout band* for each OpSim map, and set the LBG magnitude cuts:

$$\begin{aligned} u\text{-drop.}: \quad r_{\text{cut}} &= \min(u_3) - 1 = \min(u_5) - 0.45 \\ g\text{-drop.}: \quad i_{\text{cut}} &= \min(g_3) - 1 = \min(g_5) - 0.45, \end{aligned} \quad (16)$$

where we have used

$$m_3 = m_5 + 2.5 \log_{10} \frac{5}{3} \approx m_5 + 0.55, \quad (17)$$

and the minimum is taken over pixels in the OpSim map.

For r and i -dropouts, the dropout band is deeper than the detection band (z and y , respectively). For these samples, therefore, we select the deepest 75% of pixels in the

detection band for each OpSim map, and set the LBG magnitude cuts:

$$\begin{aligned} r\text{-dropouts}: \quad z_{\text{cut}} &= \min(z_5) \\ i\text{-dropouts}: \quad y_{\text{cut}} &= \min(y_5) \\ z\text{-dropouts}: \quad y_{\text{cut}} &= \min(y_5). \end{aligned} \quad (18)$$

For example, the cuts for the baseline v3.6 survey strategy in year 1 (10) are

$$\begin{aligned} u\text{-dropouts}: \quad r_{\text{cut}} &= 23.48 \quad (24.72) \\ g\text{-dropouts}: \quad i_{\text{cut}} &= 24.64 \quad (26.00) \\ r\text{-dropouts}: \quad z_{\text{cut}} &= 24.18 \quad (25.57) \\ i\text{-dropouts}: \quad y_{\text{cut}} &= 24.18 \quad (25.57) \\ z\text{-dropouts}: \quad y_{\text{cut}} &= 23.33 \quad (24.63), \end{aligned}$$

where, again, the minimum is taken over pixels in the OpSim map.

Using these values for m_{cut} , we evaluate Equation 15 across the OpSim map (keeping only the deepest 75% of pixels) and take the mean. This mean density is the metric used to compare LBG detection for different survey strategies. Note that while m_{cut} is set for the entire sample, m_5 varies spatially across the survey footprint due to spatial variation in observing quality. Even within this deepest 75%, non-uniformity of LBG number densities due to spatial modulation of m_5 will be important for studies of large-scale structure, as this modulation in number density can be mistaken as large scale structure ([Weaverdyck & Huterer 2021](#)). We will investigate the impact of this modulation on forecasts for LSST cosmology in future work. We also do not model contamination by low-redshift interlopers, the impact of which are discussed in Section 5.

4. RESULTS

4.1. Photo- z Estimation

We use the CMNN algorithm to estimate photo- z 's for every galaxy in the simulated $z \leq 3.5$ catalog, using OpSim maps of *ugrizy* 5σ depths for LSST year 10. We quantify photo- z accuracy via the quantity $\Delta z = (z_{\text{phot}} - z_{\text{true}})/(1 + z_{\text{true}})$, the numerator of which quantifies the photo- z error, while the denominator compensates for the larger uncertainty at high redshifts. We then bin galaxies by true redshift and calculate the following quantities for each bin:

- the robust standard deviation, $\sigma_{\Delta z}$, which we define as the width of the interquartile range (IQR) of Δz , divided by 1.349 to convert to the equivalent of a Gaussian standard deviation;
- the photo- z bias, which we define as the mean value of Δz for galaxies within the IQR;

⁷ Equation 16 below makes clear the criterion for being ‘‘sufficiently deep’’ is that the 5σ depth in the dropout band is more than 0.45 magnitudes deeper than the 5σ depth in the detection band. See Table 2 for the relative depth of each band.

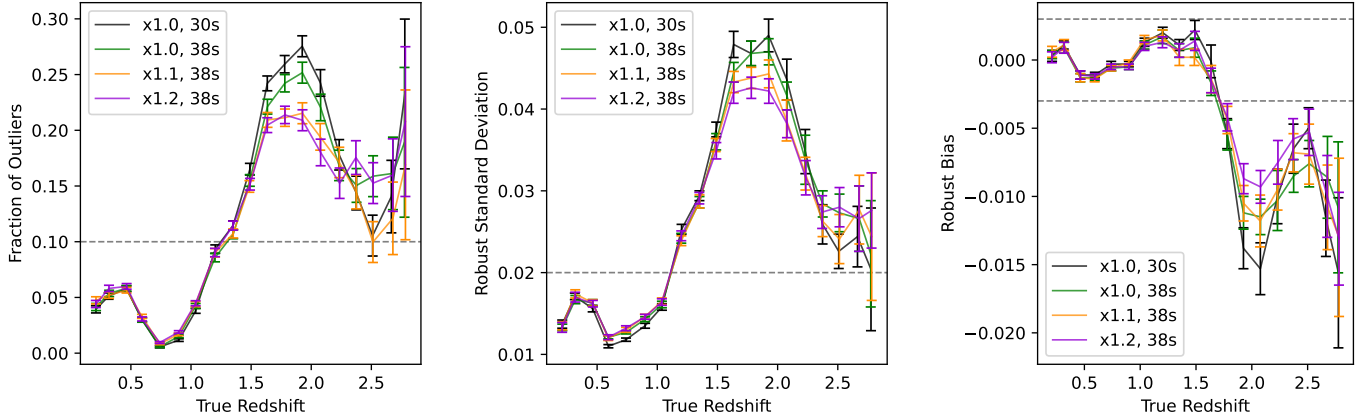


Figure 6. Photo- z metrics for simulations of several different u -band survey strategies. For clarity, we plot only a small subset of the u -band strategies considered. Each panel displays the corresponding requirement for LSST science as a horizontal gray line (Ivezić & the LSST Science Collaboration 2018). These requirements provide a sense of scale for each metric, but whether or not this photo- z estimator achieves each limit in different redshift ranges is not predictive of the photo- z performance of DESC cosmology, due to the considerations discussed in Section 3.1.

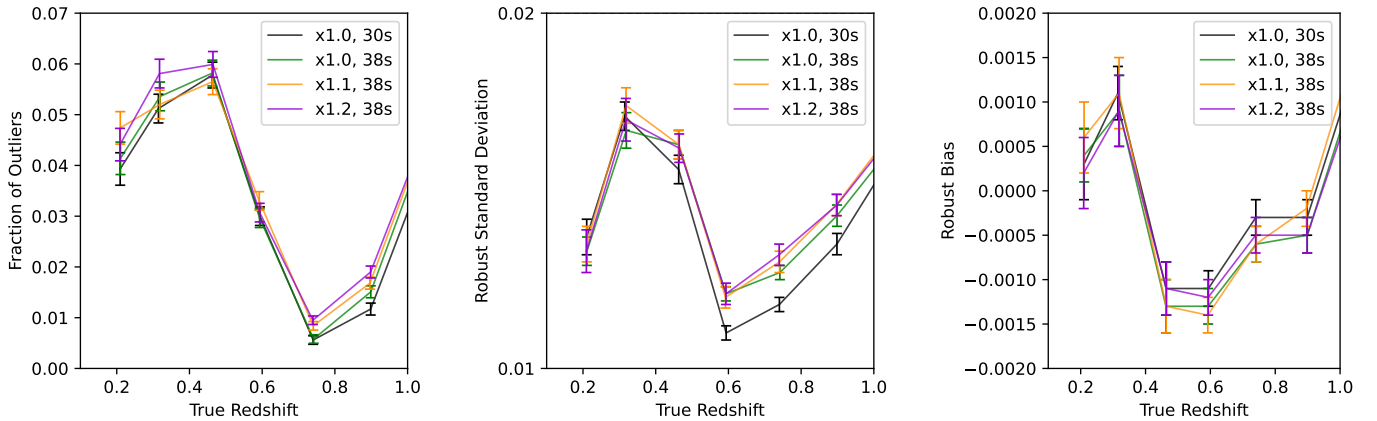


Figure 7. Same as Fig. 6, zoomed in on the $z < 1$ region for each metric.

- the outlier fraction, which we define as the fraction of galaxies for which $|\Delta z| > 3\sigma_{\Delta z}$.

When calculating the first two quantities, we exclude the galaxies that are flagged as outliers, so these two quantities characterize the core of the distribution, while the outlier fraction characterizes the tails.

These quantities, as a function of redshift, are plotted in Fig. 6, with the colors corresponding to different u -band strategies (recall Section 2.1 and Table 2). All three metrics significantly degrade above $z \sim 1.2$, at which point the Balmer break redshifts out of the Rubin bandpasses and there is relatively little information present in galaxy spectra for broadband photo- z estimation, resulting in significantly degraded photo- z accuracy (LSST Science Collaboration et al. 2009; Kalmbach et al. 2020). Around $z \sim 1.6$, however, Lyman-series transitions (i.e., the Lyman-alpha forest) begin to redshift into the Rubin u band, stealing progressively more of the u -band flux.

This provides a distinctive signal for photo- z estimation, resulting in a reversal of the trend, with photo- z accuracy improving until about $z \sim 2.5$. Our simulations contain very few galaxies beyond this redshift, resulting in increased photo- z errors and uncertainties in the quantities plotted in Fig. 6.

For all three quantities, increasing the total u -band exposure time improves photo- z results in the range $1.5 < z < 2.5$: the outlier fraction improves by up to 30%; the standard deviation improves by up to 20%; the bias improves by up to 40%. These improvements are due to the greater u -band depth increasing the SNR of the u -band flux decrement that results from the redshifting of Lyman-series absorption into the Rubin u band.

The improvements in photo- z estimation at $1.5 < z < 2.5$, however, come with a loss of performance at $z < 1$ due to the decreased depth in the *grizy* bands (because more time spent observing in u must result in less time observing in *grizy*, due to the fixed 10-year duration

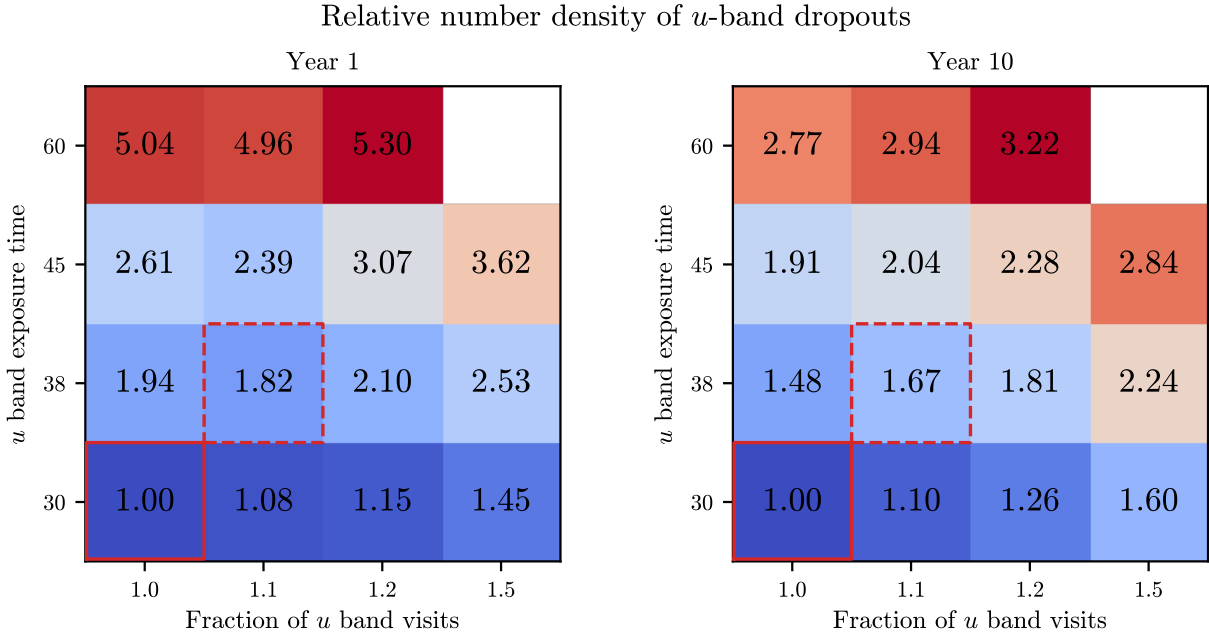


Figure 8. Relative number density of $z \sim 3$ u -band dropouts detected across the deepest 75% of the survey footprint for different simulations of u -band survey strategy. Left panel corresponds to LSST year 1, right panel to year 10. The block corresponding to baseline v3.4, [1.0x, 30s u], is bordered by a solid red box, while the SCOC recommendation of [1.1x, 38s u] is bordered by a dashed red box. The absolute number density for baseline v3.4 is 69 deg^{-2} in year 1 and 2113 deg^{-2} in year 10.

of LSST). The three panels of Fig. 7 show the same quantities as Fig. 6, zoomed in on the region $z < 1$. These losses, while smaller in magnitude than the gains at $1.5 < z < 2.5$, are, however, statistically significant, especially for the outlier fraction and scatter, which both degrade by up to 3σ . It must also be kept in mind that the $z < 1$ galaxy sample contains far more galaxies, both in our simulations and for the future LSST survey. Thus these small performances losses at $z < 1$ may be judged to outweigh the gains at $1.5 < z < 2.5$, depending on the science case in consideration.

We note, however, that our simulated photometry, while noisy, is free of biases, aperture corrections, and other systematic errors. These effects, present in real measured photometry, are likely to erase the small changes in photo- z performance at $z < 1$ that result from the small changes in *grizy* depth (cf. Table 2). We judge, therefore, that the impressive gains at $z > 1.5$ provide strong motivation for increasing u -band observing time. Indeed, baselines v3.5 onward have adopted the [1.1x, 38s u] strategy, partially as a result of the findings presented here.

4.2. LBG Detection

We forecast LBG detection for each survey simulation using the strategy described in Section 3.2, considering first only u -band dropouts, which provide LBG samples

at $z \sim 3$. We discuss the higher-redshift *griz* dropouts at the end of this section.

For the deepest 75% of the survey footprint in baseline v3.4, we forecast a u -band dropout number density of 69 deg^{-2} in year 1 and 2113 deg^{-2} in year 10. Relative LBG number densities for the range of u -band strategy simulations are displayed in Fig. 8. Increasing u -band depth by increasing the number of u -band visits and/or the u -band per-visit exposure time results in a greater number density of detected LBGs due to the correspondingly deeper cut that is allowed in the detection band (the r band; cf. Equation 16).

Note that for a fixed increase in total u -band observing time, increasing the per-visit exposure time has a greater impact than increasing the number of u -band visits. For example, the [1.5x, 30s u] and [1.0x, 45s u] both correspond to increasing the total u -band observing time by 50%, but the latter strategy with longer per-visit exposures results in a much greater increase in LBG number density. This is because the Rubin u band is read-noise limited due to the lower sky background at these wavelengths. Indeed, the impact of a 10% increase in the number of u -band visits is so marginal that the potential for extra accumulated u -band depth is not sufficient by the end of year 1 to overcome natural depth variations between different simulation realizations. Thus, the “1.1” column in the left panel of Fig. 8 reports lower LBG number densities than the “1.0” column. This discrep-

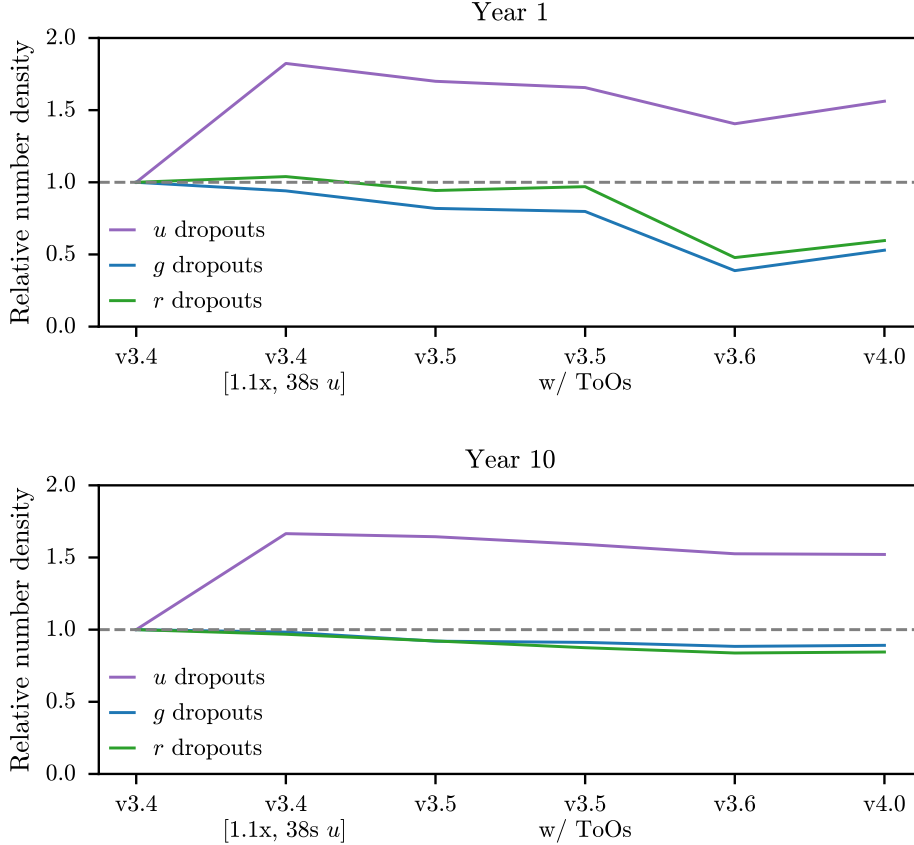


Figure 9. Evolution of u -, g -, and r -band dropouts for a series of subsequent survey simulations. v3.4 is the baseline simulation after the adoption of the new Ag-Ag-Ag mirror coatings. v3.4 [1.1x, 38s u] is the same as v3.4, except with 10% more visits in the u band, with a per-visit exposure time of 38 seconds (compared to 30 seconds in baseline v3.4). v3.5 is the new baseline after the adoption of the [1.1x, 38s u] strategy, and includes a few other changes. v3.5 w/ ToOs is the same as baseline v3.5, except with some survey time dedicated to Target of Opportunities. Baselines v3.6 and v4.0 include more realistic simulations of year 1 observatory downtime.

ancy also provides an estimate for the precision of our estimated LBG number densities, when considering uncertainties due to natural variations between different simulation realizations.

Another important feature to recognize is that the proposed increases to u -band depth have a larger impact in year 1 than in year 10 when comparing relative number of LBGs detected. Compare, for example, the relative LBG number density increase for the most aggressive u -band strategy, which increases the number of u -band visits by 20% and the u -band exposure time to 60 seconds. In year 10, this strategy results in $3.2\times$ more LBGs detected, a large increase that is, however, much smaller than the corresponding $5.3\times$ increase in year 1. This is because year 1 depths are on a steeper part of the LBG luminosity function compared to the deeper year 10 depths (cf. Fig. 5), so the increase in LBG number density per unit depth is greater in year 1 than in year 10.

In October 2024 the Rubin SCOC recommended that LSST adopt the [1.1x, 38s u] strategy for the u band (Rubin Observatory Survey Cadence Optimization Committee 2024). Note with this strategy and the Ag-Ag-Ag mirror coatings, all bands are deeper than under the previous Al-Ag-Al baseline. This strategy, marked by the dashed-red boxes in Fig. 8, was incorporated into the new baseline simulation, v3.5. Baseline simulations v3.5, v3.6, and v4.0 include other changes, unrelated to u -band strategy, that also impact forecast LBG number densities, including dedicating survey time to targets of opportunity⁸ (ToOs), as well as increasing the amount of year 1 observatory down-time to more realistic levels. The impacts of these changes to survey strategy on the detection of LBGs are shown in Fig. 9.

⁸ ToOs are transient events, such as gravitational wave detections (Cowperthwaite et al. 2019), that require immediate follow-up observations.

Table 3. Forecast LBG number densities for year 1 (10) of LSST assuming survey strategy baseline v4.0.

Field	n_u	n_g	n_r	n_i	n_z
WFD	110 (3200)	400 (6300)	4.4 (230)	0.19 (9.9)	0.01 (0.44)
COSMOS	9400 (13000)	13000 (27000)	1100 (2700)	120 (360)	0.74 (5.1)
ECDFS	5400 (13000)	6900 (23000)	260 (2300)	23 (290)	0.25 (4.3)
ELAIS S1	3000 (13000)	4700 (22000)	340 (1700)	29 (210)	0.17 (2.0)
XMM-LSS	4400 (11000)	4400 (18000)	220 (1600)	19 (190)	0.14 (2.3)
EDFS	2000 (15000)	5400 (25000)	280 (2400)	20 (310)	0.23 (3.8)

NOTE—All number densities are in units of deg^{-2} , rounded to 2 significant digits.

In year 1, the number of detected u -band dropouts is seen to increase by a factor of 1.8 under strategy [1.1x, 38s u], an increase that is mostly sustained across baseline v3.5 and the subsequent inclusion of ToOs. There is a significant decrease in u -band dropout detection in baseline v3.6 due to the more realistic amount of observatory downtime simulated in year 1. This decrease is somewhat mitigated by the improvements to simulating year 1 downtime implemented in baseline v4.0 (see Section 2.1). A similar pattern is visible for year 10 detections, however the decrease in LBG number densities due to the increased year 1 downtime is far smaller, due to this comprising a much smaller fraction of survey time by year 10.

In both panels we also plot the forecast number density of g - and r -band dropouts, at redshifts $z \sim 4$ and $z \sim 5$, respectively. It is seen that the chosen increase to u -band survey time results in only very modest reductions in the number densities of these higher-redshift LBGs. While not shown in the plots, the same is true of z - and y -band dropouts, at redshifts $z \sim 6$ and $z \sim 7$, respectively. Number densities for all dropout samples for the baseline v4.0 survey strategy are shown in Fig. 5.

Finally, we list projected LBG number densities for simulation baseline v4.0 in Table 3. Densities are listed for years 1 and 10, including the WFD survey and all LSST deep fields. Note that densities are much greater in COSMOS in year 1, compared to the other deep fields, reflecting the early emphasis on building depth in COSMOS for photo- z calibration and low-surface-brightness science.

5. CONCLUSIONS

This paper used OpSim simulations of the LSST survey, together with simple models of IGM absorption and LBG dropout detection, to evaluate the impact of LSST u -band observing strategy on photo- z estimation and detection of LBGs. We find that:

- Adjusting LSST strategy to increase u -band depth has a small, but statistically-significant negative impact on photo- z estimation for galaxies at $z < 1.5$. We expect these small changes in performance, however, would be erased by a more realistic treatment of photometry that includes systematic errors, such as aperture corrections.
- For galaxies at $z > 1.5$, increasing the u -band depth yields a significant improvement in photo- z estimation.
- Increasing u -band depth has the potential to dramatically increase the number of $z \sim 3$ u -band dropouts detected by LSST.

These metrics were presented to the Rubin SCOC in June 2024, motivating the SCOC to recommend increasing the number of u -band visits by 10% and the per-visit exposure time to 38 seconds (Rubin Observatory Survey Cadence Optimization Committee 2024), which has been adopted as the baseline for survey strategy simulations going forward. With this strategy and the Ag-Ag-Ag mirror coatings, the projected depths in all six bands are deeper than the previous Al-Ag-Al baseline.

With the adoption of this u -band strategy, our metrics indicate that

- The outlier fraction, standard deviation, and bias of $z < 1.5$ galaxies will *increase* by 20%, 5%, and 50%, respectively. These values are, however, small in absolute magnitude, and all three metrics remain well below the LSST requirements.
- The outlier fraction, standard deviation, and bias of $z > 1.5$ galaxies will *decrease* by up to 28%, 10%, and 25%, respectively. As all three metrics are significantly larger at high-redshifts, these also represent large improvements in absolute value.

- The number density of u -band dropouts will increase by 82% in year 1 and 67% in year 10. Forecast number densities for $ugriz$ -dropouts in the LSST WFD and DDFs are listed in Table 3.

This represents significant gains for science with high-redshift galaxies. For example, the u -band dropout sample forecast to have number densities of 110 deg^{-2} (3200 deg^{-2}) in year 1 (10) will enable measurement of the cross-correlation with Simons Observatory CMB lensing at an SNR of 90 (160) (Wilson & White 2019; Ade et al. 2019). Such powerful constraints on high-redshift large-scale structure will enable 1% constraints on the high-redshift evolution of σ_8 (Wilson & White 2019), competitive constraints on the amplitude of local-type primordial non-Gaussianity (Schmittfull & Seljak 2018; Chaussidon et al. 2024), optical-depth-independent constraints on the sum of neutrino masses (Yu et al. 2018), and high-precision constraints on the masses of $z > 1$ clusters (Tudorica et al. 2017).

Given the high SNR forecast for our observables, the precision of cosmological constraints will ultimately be limited by our control of systematic errors. One of the most important sources for systematic error to consider is photo- z contamination from low-redshift interlopers. Galaxies with strong Balmer/4000 Å breaks, dusty galaxies, emission line galaxies (ELGs), and low-temperature dwarf stars all contaminate LBG dropout samples because they have colors that mimic the Lyman break (Stanway et al. 2008; Reddy et al. 2008; Vulcani et al. 2017; Ono et al. 2018). Indeed, Ruhlmann-Kleider et al. (2024) and Payerne et al. (2024) found the purity of u -band dropout samples depends strongly on u -band depth, with the number of low-redshift interlopers dropping by 38% as u -band depth increases from 24.5 to 25.5. Furthermore, deep u -band imaging is valuable for suppressing interlopers in high-redshift dropout populations by rejecting sources with non-negligible flux in wavelengths bluer than the supposed dropout band (Vulcani et al. 2017). Thus, while this paper considers only detected number densities of true LBGs, greater u -band depth will also increase purity for LBG dropout samples at all redshifts. The deep photometry and data at other wavelengths available in the LSST DDFs will be invaluable for characterizing interloper populations present in LSST LBG dropout samples. Careful study and calibration of these populations will be necessary to enable precision cosmology with LBGs detected by LSST.

Finally, we note that increasing the u -band depth of LSST imaging enhances synergies with the proposed DESI-II survey (Schlegel et al. 2022), the extension of Dark Energy Spectroscopic Instrument (DESI) (DESI Collaboration et al. 2016) which aims to map the 3D

matter distribution in the $2 < z < 4$ universe using spectroscopic samples of LBGs and Lyman-alpha emitters (LAEs), enabling tests of cosmological models in the matter-dominated era. DESI-II plans to use LSST year 2 catalogs to select candidate LBGs and LAEs for spectroscopic follow-up. As previously discussed, increasing LSST u -band depth will increase the number density and purity of these candidate samples, increasing the efficiency of the DESI-II survey.

The code to produce the plots in this paper are available on GitHub⁹. The code for the LBG models described in Section 2.3 are published as the python package `lbg_tools`¹⁰, which is available on PyPI¹¹.

ACKNOWLEDGEMENTS

We thank Yoshiaki Ono for providing HSC completeness curves. This paper has undergone internal review by the LSST Dark Energy Science Collaboration. The internal reviewers were Sam Schmidt and Rebecca Chen. The authors thank the internal reviewers for their valuable comments.

JFC acknowledges support from the U.S. Department of Energy, Office of Science, Office of High Energy Physics Cosmic Frontier Research program under Award Number DE-SC0011665. EG acknowledges support from the U.S. Department of Energy, Office of Science, Office of High Energy Physics Cosmic Frontier Research program under Award Number DE-SC0010008 and from an IBM Einstein fellowship for his sabbatical at IAS during the completion of this manuscript. AIM acknowledges the support of Schmidt Sciences. BL is supported by the Royal Society through a University Research Fellowship.

Author contributions are as follows. JFC designed the LBG metrics, performed the analysis, and wrote the majority of the paper. BL proposed the idea to create LBG survey strategy metrics, developed prototypes, and provided feedback on the text. MG produced the photo- z metrics and provided feedback on the text. CP provided significant feedback on all aspects of the text and contributed connections with DESI. AJC suggested approaches and designed the CMNN photo- z estimator. EG suggested approaches and provided feedback on the text. TK provided input on aspects of LBG cosmology and connections to DESI. AIM contributed to the photo- z metrics. JN suggested approaches and provided feedback on metrics. MR provided feedback on LBG cosmology, including relevance to cluster cosmology.

⁹ <https://github.com/jfcrenshaw/u-band-strat>

¹⁰ https://github.com/jfcrenshaw/lbg_tools

¹¹ <https://pypi.org/project/lbg-tools/>

The DESC acknowledges ongoing support from the Institut National de Physique Nucléaire et de Physique des Particules in France; the Science & Technology Facilities Council in the United Kingdom; and the Department of Energy, the National Science Foundation, and the LSST Corporation in the United States. DESC uses resources of the IN2P3 Computing Center (CC-IN2P3–Lyon/Villeurbanne - France) funded by the Centre National de la Recherche Scientifique; the National Energy Research Scientific Computing Center, a DOE Office of Science User Facility supported by the Office of Science of the U.S. Department of Energy under Contract No. DE-AC02-05CH11231; STFC DiRAC HPC Facilities, funded by UK BEIS National E-infrastructure capital grants; and the UK particle physics grid, supported by

the GridPP Collaboration. This work was performed in part under DOE Contract DE-AC02-76SF00515.

This research has made use of NASA’s Astrophysics Data System. Software citation information aggregated using [The Software Citation Station](#) (Wagg & Broekgaarden 2024; Wagg et al. 2024).

Software: [astropy](#) (Astropy Collaboration et al. 2013, 2018, 2022), [CMNN](#) (Graham et al. 2018, 2020), [HEALPix](#) (Górski et al. 2005) and [healpy](#) (Zonca et al. 2019), [jupyter](#) (Kluyver et al. 2016), [MAF](#) (Jones et al. 2014), [matplotlib](#) (Hunter 2007), [numpy](#) (Harris et al. 2020), [pandas](#) (Wes McKinney 2010; Reback et al. 2020), [python](#) (Van Rossum & Drake 2009), [scipy](#) (Virtanen et al. 2020),

APPENDIX

A. COMMENTS ON β_{UV} DEPENDENCE OF IGM INCREMENTS Δm_{wIGM}

Note the shapes of IMG transmission curves in Figure 3 provide some insight into the effect of the UV slope. When the Lyman-alpha forest starts to redshift into a band, bluer spectra will have a larger IGM correction, Δm_{IGM} , as they have greater flux in the wavelength range impacted by extinction. However, as IGM extinction redshifts farther into the band, redder spectra will have a larger correction, as the IGM has a greater optical depth at high redshift, corresponding to longer wavelengths. You can see this from the deeper troughs on the right side of the IGM extinction curves in Figure 3. However, once the Lyman limit redshifts into the band, bluer spectra will once again have larger corrections as the IGM is far more opaque at wavelengths below the Lyman limit.

Figure 10 plots Δm_{IGM} for the u - and g -bands as a function of both redshift and UV slope. It is difficult to see the structure described above, however, indicating that these effects are relatively small.

B. FITTING THE β_{UV} MODEL

To model the UV spectra of LBGs we use HST data from [Bouwens et al. \(2014\)](#). Specifically, we use the linear fit parameters listed in Table 3 for six tomographic redshift bins between $2.5 \lesssim z \lesssim 8.0$. These parameters, as a function of mean redshift, are plotted in Fig. 11.

The parameter β_{UV} at $M_{UV} = -19.5$ show a clear linear trend with redshift, so we fit a linear model, yielding the relation

$$\beta_{UV}|_{M_{UV}=-19.5} = -0.063z - 1.61. \quad (\text{B1})$$

The parameter $d\beta_{UV}/dM_{UV}$ does not show a clear trend, so we simply take the average:

$$\left\langle \frac{d\beta_{UV}}{dM_{UV}} \right\rangle = -0.167. \quad (\text{B2})$$

Together, these two relations yield the bilinear model

$$\beta_{UV}(M, z) = -0.167(M + 19.5) - 0.063z - 1.61, \quad (\text{B3})$$

which is also printed as Eq. 10.

C. DETAILS OF THE LBG COMPLETENESS MODEL

The LBG completeness models of [Malkan et al. \(2017\)](#); [Ono et al. \(2018\)](#); [Harikane et al. \(2022\)](#) were calibrated using synthetic source injection (SSI). That is, synthetic galaxy images with a variety of spectral types, redshifts, and intrinsic magnitudes were injected into real images, and these images were processed using the usual science pipelines used for these studies. The fraction of true LBGs injected into the images were then compared with the number of LBGs that were detected in the images and then passed the corresponding color cuts. The completeness was then calculated in bins of redshift and apparent magnitude.

Estimates for u -dropout completeness come from [Malkan et al. \(2017\)](#). This study used photometry from the Subaru Deep Field, and detected LBGs using z -band imaging with 5σ depth 26.07. While we use these same completeness curves, we assume u -dropout detection occurs in the r -band, which for LSST has a 5σ depth ~ 25.7 in year 1 and ~ 26.8 in year 10, which is well-matched to the z -band depth from the Subaru Deep Field. Estimates for $griz$ -dropout completeness come from [Ono](#)

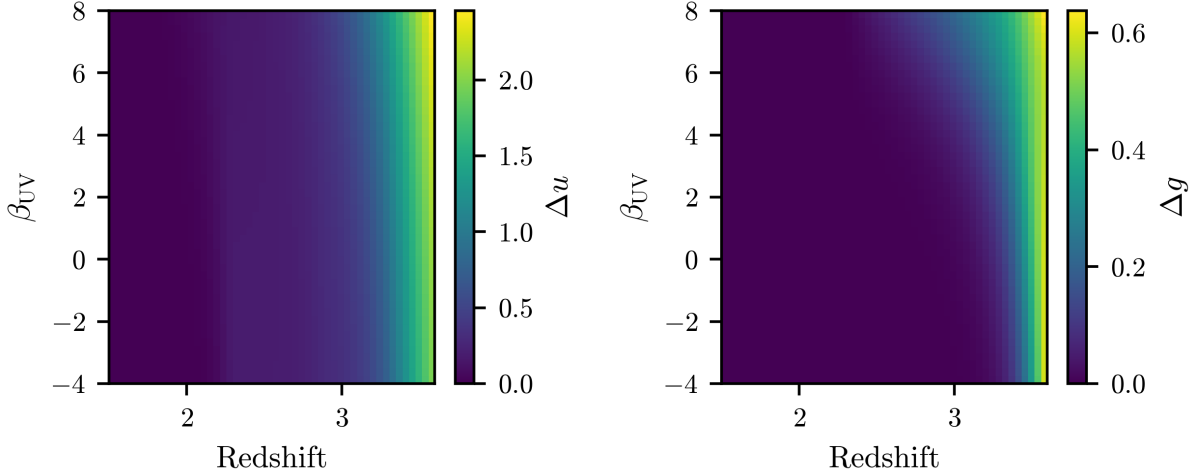


Figure 10. IGM magnitude increments for the Rubin u and g bands, as a function of source redshift and UV slope.

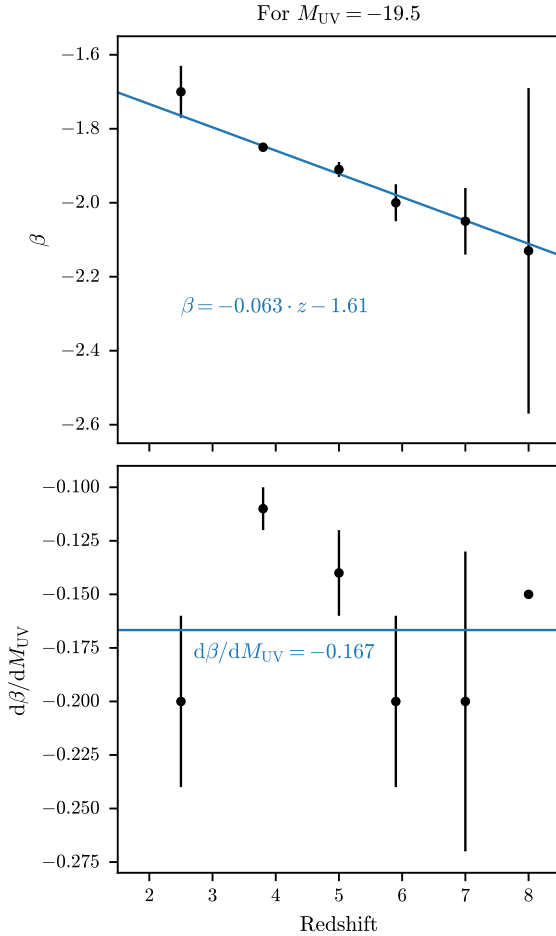


Figure 11. Parameters for the evolution of β_{UV} , taken from Table 3 of (Bouwens et al. 2014).

et al. (2018); Harikane et al. (2022), which use photometry from the HSC SSP Wide, Deep, and Ultra-deep fields. These fields span a range of 5σ depths that bracket the expected LSST year 1 and 10 depths.

In every case, we use the strategy of Harikane et al. (2022) to “rescale” completeness estimates to imaging of different depths. That is, we take the input grid of redshift, apparent magnitude, and completeness values, $\{z, m, C\}$, and subtract the 5σ depth from the apparent magnitudes:

$$\{z, m, C\} \rightarrow \{z, m - m_5, C\}. \quad (\text{C4})$$

Completeness, therefore, is modeled as a function of redshift and *magnitude relative to the 5σ depth in the detection band*. We then linearly interpolate (and extrapolate) using this grid, with completeness values clipped to the range $[0, 1]$ to keep completeness for very bright (faint) galaxies ≤ 1 (≥ 0). We smooth the input completeness curves by requiring that interpolated/extrapolated completeness values decrease monotonically with magnitude and is unimodal with respect to redshift. This improves the behavior of extrapolation beyond the input calibration grid. The “smoothed” curves are displayed in Fig 4.

Note we do not expect these completeness models to be correct *in detail* for LSST, however we do expect they provide reasonable estimates for the order of magnitude of LBGs that LSST will detect, reasonable redshift ranges for these detections, and a reasonable scaling with LBG magnitude relative to the 5σ depth of the imaging. Quantifying completeness in detail for LSST will be vital for cosmology with LBGs detected by Rubin, however we do not think these details impact the conclusions of this paper.

Finally, we note that Equation 15 uses absolute magnitudes at 1500 \AA , M , rather than apparent magnitudes, m . Equations 9-12, however, provide a fully-determined analytic model for $m = m(M, z)$. These equations can

be numerically inverted to provide a fully-determined model for $M = M(m, z)$.

REFERENCES

- Adams, N. J., Bowler, R. A. A., Jarvis, M. J., et al. 2020, *MNRAS*, 494, 1771, doi: [10.1093/mnras/staa687](https://doi.org/10.1093/mnras/staa687)
- Ade, P., Aguirre, J., Ahmed, Z., et al. 2019, *JCAP*, 2019, 056, doi: [10.1088/1475-7516/2019/02/056](https://doi.org/10.1088/1475-7516/2019/02/056)
- Aihara, H., AlSayyad, Y., Ando, M., et al. 2019, *PASJ*, 71, 114, doi: [10.1093/pasj/psz103](https://doi.org/10.1093/pasj/psz103)
- Astropy Collaboration, Robitaille, T. P., Tollerud, E. J., et al. 2013, *A&A*, 558, A33, doi: [10.1051/0004-6361/201322068](https://doi.org/10.1051/0004-6361/201322068)
- Astropy Collaboration, Price-Whelan, A. M., Sipőcz, B. M., et al. 2018, *AJ*, 156, 123, doi: [10.3847/1538-3881/aabc4f](https://doi.org/10.3847/1538-3881/aabc4f)
- Astropy Collaboration, Price-Whelan, A. M., Lim, P. L., et al. 2022, *ApJ*, 935, 167, doi: [10.3847/1538-4357/ac7c74](https://doi.org/10.3847/1538-4357/ac7c74)
- Bianco, F. B., Ivezić, Ž., Jones, R. L., et al. 2022, *ApJS*, 258, 1, doi: [10.3847/1538-4365/ac3e72](https://doi.org/10.3847/1538-4365/ac3e72)
- Bouwens, R. J., Illingworth, G. D., van Dokkum, P. G., et al. 2022, *ApJ*, 927, 81, doi: [10.3847/1538-4357/ac4791](https://doi.org/10.3847/1538-4357/ac4791)
- Bouwens, R. J., Illingworth, G. D., Oesch, P. A., et al. 2014, *The Astrophysical Journal*, 793, 115, doi: [10.1088/0004-637X/793/2/115](https://doi.org/10.1088/0004-637X/793/2/115)
- Bouwens, R. J., Oesch, P. A., Stefanon, M., et al. 2021, *The Astronomical Journal*, 162, 47, doi: [10.3847/1538-3881/abf83e](https://doi.org/10.3847/1538-3881/abf83e)
- Chaussidon, E., Yèche, C., de Mattia, A., et al. 2024, arXiv e-prints, arXiv:2411.17623, doi: [10.48550/arXiv.2411.17623](https://doi.org/10.48550/arXiv.2411.17623)
- Chen, R., Scolnic, D., Rozo, E., et al. 2022, *The Astrophysical Journal*, 938, 62, doi: [10.3847/1538-4357/ac8b82](https://doi.org/10.3847/1538-4357/ac8b82)
- Chen, R., Scolnic, D., Vincenzi, M., et al. 2024, Evaluating Cosmological Biases Using Photometric Redshifts for Type Ia Supernova Cosmology with the Dark Energy Survey Supernova Program, doi: [10.48550/arXiv.2407.16744](https://doi.org/10.48550/arXiv.2407.16744)
- Cowperthwaite, P. S., Villar, V. A., Scolnic, D. M., & Berger, E. 2019, *ApJ*, 874, 88, doi: [10.3847/1538-4357/ab07b6](https://doi.org/10.3847/1538-4357/ab07b6)
- Crenshaw, J. F., Kalmbach, J. B., Gagliano, A., et al. 2024, *The Astronomical Journal*, 168, 80, doi: [10.3847/1538-3881/ad54bf](https://doi.org/10.3847/1538-3881/ad54bf)
- Cross, D. N., & Sánchez, C. 2024, Inverse Galaxy-Galaxy Lensing: Magnification, Intrinsic Alignments and Cosmology, doi: [10.48550/arXiv.2410.00714](https://doi.org/10.48550/arXiv.2410.00714)
- DESI Collaboration, Aghamousa, A., Aguilar, J., et al. 2016, arXiv e-prints, arXiv:1611.00037, doi: [10.48550/arXiv.1611.00037](https://doi.org/10.48550/arXiv.1611.00037)
- Dunlop, J. S. 2013, in *Astrophysics and Space Science Library*, Vol. 396, *The First Galaxies*, ed. T. Wiklind, B. Mobasher, & V. Bromm, 223, doi: [10.1007/978-3-642-32362-1_5](https://doi.org/10.1007/978-3-642-32362-1_5)
- Euclid Collaboration, Adam, R., Vannier, M., et al. 2019, *A&A*, 627, A23, doi: [10.1051/0004-6361/201935088](https://doi.org/10.1051/0004-6361/201935088)
- Finkelstein, S. L., & Bagley, M. B. 2022, *The Astrophysical Journal*, 938, 25, doi: [10.3847/1538-4357/ac89eb](https://doi.org/10.3847/1538-4357/ac89eb)
- Finkelstein, S. L., Ryan, Russell E., J., Papovich, C., et al. 2015, *ApJ*, 810, 71, doi: [10.1088/0004-637X/810/1/71](https://doi.org/10.1088/0004-637X/810/1/71)
- Finkelstein, S. L., Bagley, M. B., Ferguson, H. C., et al. 2022, CEERS Key Paper I: An Early Look into the First 500 Myr of Galaxy Formation with JWST, arXiv, doi: [10.48550/arXiv.2211.05792](https://doi.org/10.48550/arXiv.2211.05792)
- Giavalisco, M. 2002, *ARA&A*, 40, 579, doi: [10.1146/annurev.astro.40.121301.111837](https://doi.org/10.1146/annurev.astro.40.121301.111837)
- Gonzalez-Perez, V., Lacey, C. G., Baugh, C. M., et al. 2014, *Monthly Notices of the Royal Astronomical Society*, 439, 264, doi: [10.1093/mnras/stt2410](https://doi.org/10.1093/mnras/stt2410)
- Górski, K. M., Hivon, E., Banday, A. J., et al. 2005, *ApJ*, 622, 759, doi: [10.1086/427976](https://doi.org/10.1086/427976)
- Graham, M. L., Connolly, A. J., Ivezić, Ž., et al. 2018, *The Astronomical Journal*, 155, 1, doi: [10.3847/1538-3881/aa99d4](https://doi.org/10.3847/1538-3881/aa99d4)
- Graham, M. L., Connolly, A. J., Wang, W., et al. 2020, *The Astronomical Journal*, 159, 258, doi: [10.3847/1538-3881/ab8a43](https://doi.org/10.3847/1538-3881/ab8a43)
- Hang, Q., Joachimi, B., Charles, E., et al. 2024, *Monthly Notices of the Royal Astronomical Society*, doi: [10.1093/mnras/stae2519](https://doi.org/10.1093/mnras/stae2519)
- Harikane, Y., Ono, Y., Ouchi, M., et al. 2022, *The Astrophysical Journal Supplement Series*, 259, 20, doi: [10.3847/1538-4365/ac3dfc](https://doi.org/10.3847/1538-4365/ac3dfc)
- Harikane, Y., Ouchi, M., Oguri, M., et al. 2023, *The Astrophysical Journal Supplement Series*, 265, 5, doi: [10.3847/1538-4365/acaaa9](https://doi.org/10.3847/1538-4365/acaaa9)
- Harris, C. R., Millman, K. J., van der Walt, S. J., et al. 2020, *Nature*, 585, 357, doi: [10.1038/s41586-020-2649-2](https://doi.org/10.1038/s41586-020-2649-2)
- Hunter, J. D. 2007, *Computing in Science & Engineering*, 9, 90, doi: [10.1109/MCSE.2007.55](https://doi.org/10.1109/MCSE.2007.55)
- Inoue, A. K., Shimizu, I., Iwata, I., & Tanaka, M. 2014, *Monthly Notices of the Royal Astronomical Society*, 442, 1805, doi: [10.1093/mnras/stu936](https://doi.org/10.1093/mnras/stu936)

- Ivezić, v., & the LSST Science Collaboration. 2018, The LSST System Science Requirements Document, Vera C. Rubin Observatory. <https://docushare.lsst.org/docushare/dsweb/Get/LPM-17>
- Ivezić, Ž., Kahn, S. M., Tyson, J. A., et al. 2019, *The Astrophysical Journal*, 873, 111, doi: [10.3847/1538-4357/ab042c](https://doi.org/10.3847/1538-4357/ab042c)
- Izotov, Y. I., Guseva, N. G., Fricke, K. J., et al. 2021, *A&A*, 646, A138, doi: [10.1051/0004-6361/202039772](https://doi.org/10.1051/0004-6361/202039772)
- Jones, R. L., Yoachim, P., Ivezić, v., Neilsen, E. H. J., & Ribeiro, T. 2021, Survey Strategy and Cadence Choices for the Vera C. Rubin Observatory Legacy Survey of Space and Time (LSST), Vera C. Rubin Observatory. <https://pstn-051.lsst.io>
- Jones, R. L., Yoachim, P., Chandrasekharan, S., et al. 2014, in *Observatory Operations: Strategies, Processes, and Systems V*, ed. A. B. Peck, C. R. Benn, & R. L. Seaman, Vol. 9149, International Society for Optics and Photonics (SPIE), 91490B, doi: [10.1117/12.2056835](https://doi.org/10.1117/12.2056835)
- Kalmbach, J. B., VanderPlas, J. T., & Connolly, A. J. 2020, *The Astrophysical Journal*, 890, 74, doi: [10.3847/1538-4357/ab684f](https://doi.org/10.3847/1538-4357/ab684f)
- Kluyver, T., Ragan-Kelley, B., Pérez, F., et al. 2016, in *Positioning and Power in Academic Publishing: Players, Agents and Agendas*, ed. F. Loizides & B. Schmidt (Netherlands: IOS Press), 87–90. <https://eprints.soton.ac.uk/403913/>
- Leonard, C. D., Rau, M. M., & Mandelbaum, R. 2024, Photometric Redshifts and Intrinsic Alignments: Degeneracies and Biases in 3σ Analysis, arXiv. <https://arxiv.org/abs/2401.06060>
- Lochner, M., Scolnic, D. M., Awan, H., et al. 2018, arXiv e-prints, arXiv:1812.00515, doi: [10.48550/arXiv.1812.00515](https://doi.org/10.48550/arXiv.1812.00515)
- Lochner, M., Scolnic, D., Almoubayyed, H., et al. 2022, *ApJS*, 259, 58, doi: [10.3847/1538-4365/ac5033](https://doi.org/10.3847/1538-4365/ac5033)
- LSST Science Collaboration, Abell, P. A., Allison, J., et al. 2009, arXiv e-prints, 0912, arXiv:0912.0201. <http://adsabs.harvard.edu/abs/2009arXiv0912.0201L>
- LSST Science Collaboration, Marshall, P., Anguita, T., et al. 2017, arXiv e-prints, arXiv:1708.04058, doi: [10.48550/arXiv.1708.04058](https://doi.org/10.48550/arXiv.1708.04058)
- Malkan, M. A., Cohen, D. P., Maruyama, M., et al. 2017, *The Astrophysical Journal*, 850, 5, doi: [10.3847/1538-4357/aa9331](https://doi.org/10.3847/1538-4357/aa9331)
- Malz, A. I., Lanusse, F., Crenshaw, J. F., & Graham, M. L. 2021, An Information-Based Metric for Observing Strategy Optimization, Demonstrated in the Context of Photometric Redshifts with Applications to Cosmology, doi: [10.48550/arXiv.2104.08229](https://doi.org/10.48550/arXiv.2104.08229)
- Mason, C. A., Trenti, M., & Treu, T. 2022, The Brightest Galaxies at Cosmic Dawn. <https://ui.adsabs.harvard.edu/abs/2022arXiv220714808M>
- Merson, A. I., Baugh, C. M., Helly, J. C., et al. 2013, *Monthly Notices of the Royal Astronomical Society*, 429, 556, doi: [10.1093/mnras/sts355](https://doi.org/10.1093/mnras/sts355)
- Mitra, A., Kessler, R., More, S., Hlozek, R., & LSST Dark Energy Science Collaboration. 2023, *The Astrophysical Journal*, 944, 212, doi: [10.3847/1538-4357/acb057](https://doi.org/10.3847/1538-4357/acb057)
- Miyatake, H., Harikane, Y., Ouchi, M., et al. 2022, *Physical Review Letters*, 129, 061301, doi: [10.1103/PhysRevLett.129.061301](https://doi.org/10.1103/PhysRevLett.129.061301)
- Moutard, T., Sawicki, M., Arnouts, S., et al. 2020, *MNRAS*, 494, 1894, doi: [10.1093/mnras/staa706](https://doi.org/10.1093/mnras/staa706)
- Newman, J. A., & Gruen, D. 2022, *Annu. Rev. Astron. Astrophys.*, 60, annurev, doi: [10.1146/annurev-astro-032122-014611](https://doi.org/10.1146/annurev-astro-032122-014611)
- Newman, J. A., Abate, A., Abdalla, F. B., et al. 2015, *Astroparticle Physics*, 63, 81, doi: [10.1016/j.astropartphys.2014.06.007](https://doi.org/10.1016/j.astropartphys.2014.06.007)
- Ono, Y., Ouchi, M., Harikane, Y., et al. 2018, *Publications of the Astronomical Society of Japan*, 70, S10, doi: [10.1093/pasj/psx103](https://doi.org/10.1093/pasj/psx103)
- Parsa, S., Dunlop, J. S., McLure, R. J., & Mortlock, A. 2016, *MNRAS*, 456, 3194, doi: [10.1093/mnras/stv2857](https://doi.org/10.1093/mnras/stv2857)
- Payerne, C., d’Assignies Doumerg, W., Yèche, C., et al. 2024, High-Redshift LBG Selection from Broadband and Wide Photometric Surveys Using a Random Forest Algorithm, doi: [10.48550/arXiv.2410.08062](https://doi.org/10.48550/arXiv.2410.08062)
- Planck Collaboration, Aghanim, N., Akrami, Y., et al. 2020, *Astronomy and Astrophysics*, 641, A6, doi: [10.1051/0004-6361/201833910](https://doi.org/10.1051/0004-6361/201833910)
- Reback, J., McKinney, W., jbrockmendel, et al. 2020, *Pandas-Dev/Pandas: Pandas 1.0.3*, Zenodo. <https://doi.org/10.5281/zenodo.3715232>
- Reddy, N. A., Steidel, C. C., Pettini, M., et al. 2008, *ApJS*, 175, 48, doi: [10.1086/521105](https://doi.org/10.1086/521105)
- Rubin Observatory Survey Cadence Optimization Committee. 2022, Survey Cadence Optimization Committee’s Phase 1 Recommendations, Vera C. Rubin Observatory. <https://pstn-053.lsst.io>
- . 2023, Survey Cadence Optimization Committee’s Phase 2 Recommendations, Vera C. Rubin Observatory. <https://pstn-055.lsst.io>
- . 2024, Survey Cadence Optimization Committee’s Phase 3 Recommendations, Vera C. Rubin Observatory. <https://pstn-056.lsst.io>

- Ruhlmann-Kleider, V., Yèche, C., Magneville, C., et al. 2024, High Redshift LBGs from Deep Broadband Imaging for Future Spectroscopic Surveys, arXiv, doi: [10.48550/arXiv.2404.03569](https://doi.org/10.48550/arXiv.2404.03569)
- Sawicki, M., Arnouts, S., Huang, J., et al. 2019, Monthly Notices of the Royal Astronomical Society, 489, 5202, doi: [10.1093/mnras/stz2522](https://doi.org/10.1093/mnras/stz2522)
- Schlegel, D. J., Ferraro, S., Aldering, G., et al. 2022, arXiv e-prints, arXiv:2209.03585, doi: [10.48550/arXiv.2209.03585](https://doi.org/10.48550/arXiv.2209.03585)
- Schmidt, S. J., Malz, A. I., Soo, J. Y. H., et al. 2020, arXiv:2001.03621 [astro-ph], <https://arxiv.org/abs/2001.03621>
- Schmittfull, M., & Seljak, U. 2018, Physical Review D, 97, 123540, doi: [10.1103/PhysRevD.97.123540](https://doi.org/10.1103/PhysRevD.97.123540)
- Scott, B. R., Malz, A. I., & Sorba, R. 2024, arXiv e-prints, arXiv:2409.20443, doi: [10.48550/arXiv.2409.20443](https://doi.org/10.48550/arXiv.2409.20443)
- Springel, V., White, S. D. M., Jenkins, A., et al. 2005, Nature, 435, 629, doi: [10.1038/nature03597](https://doi.org/10.1038/nature03597)
- Stanway, E. R., Bremer, M. N., & Lehnert, M. D. 2008, MNRAS, 385, 493, doi: [10.1111/j.1365-2966.2008.12853.x](https://doi.org/10.1111/j.1365-2966.2008.12853.x)
- Steidel, C. C., Giavalisco, M., Pettini, M., Dickinson, M., & Adelberger, K. L. 1996, The Astrophysical Journal, 462, L17, doi: [10.1086/310029](https://doi.org/10.1086/310029)
- Stevans, M. L., Finkelstein, S. L., Wold, I., et al. 2018, ApJ, 863, 63, doi: [10.3847/1538-4357/aacbd7](https://doi.org/10.3847/1538-4357/aacbd7)
- The LSST Dark Energy Science Collaboration, Mandelbaum, R., Eifler, T., et al. 2018, arXiv e-prints, 1809, arXiv:1809.01669, <http://adsabs.harvard.edu/abs/2018arXiv180901669T>
- Tudorica, A., Hildebrandt, H., Tewes, M., et al. 2017, Astronomy and Astrophysics, 608, A141, doi: [10.1051/0004-6361/201731267](https://doi.org/10.1051/0004-6361/201731267)
- Van Rossum, G., & Drake, F. L. 2009, Python 3 Reference Manual (Scotts Valley, CA: CreateSpace)
- Virtanen, P., Gommers, R., Oliphant, T. E., et al. 2020, Nature Methods, 17, 261, doi: [10.1038/s41592-019-0686-2](https://doi.org/10.1038/s41592-019-0686-2)
- Vulcani, B., Trenti, M., Calvi, V., et al. 2017, The Astrophysical Journal, 836, 239, doi: [10.3847/1538-4357/aa5caf](https://doi.org/10.3847/1538-4357/aa5caf)
- Wagg, T., Broekgaarden, F., & Gültekin, K. 2024, TomWagg/software-citation-station: v1.2, v1.2, Zenodo, doi: [10.5281/zenodo.13225824](https://doi.org/10.5281/zenodo.13225824)
- Wagg, T., & Broekgaarden, F. S. 2024, arXiv e-prints, arXiv:2406.04405, <https://arxiv.org/abs/2406.04405>
- Weaverdyck, N., & Huterer, D. 2021, Monthly Notices of the Royal Astronomical Society, 503, 5061, doi: [10.1093/mnras/stab709](https://doi.org/10.1093/mnras/stab709)
- Wes McKinney. 2010, in Proceedings of the 9th Python in Science Conference, ed. S. van der Walt & Jarrod Millman, 56–61, doi: [10.25080/Majora-92bf1922-00a](https://doi.org/10.25080/Majora-92bf1922-00a)
- Wilson, M. J., & White, M. 2019, J. Cosmol. Astropart. Phys., 2019, 015, doi: [10.1088/1475-7516/2019/10/015](https://doi.org/10.1088/1475-7516/2019/10/015)
- Yu, B., Knight, R. Z., Sherwin, B. D., et al. 2018, Towards Neutrino Mass from Cosmology without Optical Depth Information, doi: [10.48550/arXiv.1809.02120](https://doi.org/10.48550/arXiv.1809.02120)
- Zhang, T., Rau, M. M., Mandelbaum, R., Li, X., & Moews, B. 2023, Monthly Notices of the Royal Astronomical Society, 518, 709, doi: [10.1093/mnras/stac3090](https://doi.org/10.1093/mnras/stac3090)
- Zonca, A., Singer, L., Lenz, D., et al. 2019, Journal of Open Source Software, 4, 1298, doi: [10.21105/joss.01298](https://doi.org/10.21105/joss.01298)
- Zuntz, J., Lanusse, F., Malz, A. I., et al. 2021, The Open Journal of Astrophysics, 4, 13, doi: [10.21105/astro.2108.13418](https://doi.org/10.21105/astro.2108.13418)